

1 **Novel EMIC Wave Propagation Pathway Through Buchsbaum Resonance and** 2 **Inter-Hemispheric Wave Interference: Swarm Observations and Modelling**

3 I. P. Pakhotin^{1,2}, I.R. Mann¹, D. Sydorenko¹, R. Rankin¹

4 ¹ Department of Physics, University of Alberta, Edmonton, Alberta, Canada

5 ² Department of Physics and Astronomy, University of Calgary, Calgary, Alberta, Canada

6 **Key Points**

- 7 - EMIC wave propagation from the magnetosphere to the ionosphere is complicated by
- 8 reflection from the Buchsbaum resonance and interference
- 9 - Waves reflected from the Buchsbaum resonance interfere to generate a coherent driver for
- 10 a secondary lower latitude field line resonance
- 11 - This generates a field-guided secondary lower-latitude peak associated with strong shear-
- 12 to-fast mode energy conversion in the ionosphere

13 **Abstract**

14 In-situ conjugate electromagnetic ion cyclotron (EMIC) waves observed by the Swarm mission
15 in both hemispheres are presented. A complex and unusual pattern of Alfvénic EMIC wave
16 energy is observed, with a mid-latitude peak close to the source at L=3.3, as well as a secondary
17 lower L-peak. A wave propagation model reveals that the secondary peak at L=1.7 may be
18 explained by wave power being redirected equatorward due to the Buchsbaum resonance,
19 crossing and interfering with the same EMIC wave power propagating equatorwards from the
20 opposite hemisphere. This interference creates a coherent equatorial driver for a low-L field
21 line resonance at the secondary peak, and which is associated with strong shear-to-fast mode
22 coupling in the ionosphere. This behavior complicates the interpretation of low-Earth orbit
23 EMIC data for applications assessing radiation belt loss. Combined LEO observations and
24 modelling enable these novel and localized magnetosphere-ionosphere EMIC wave propagation
25 pathways to be identified.

26 **Plain Language Summary**

27 Electromagnetic ion cyclotron (EMIC) waves are important in near-Earth space due to their role
28 in reducing the amount of radiation in the Earth's radiation belts following geomagnetic storms.
29 They are studied using satellites and ground observatories. Our paper reveals how these waves
30 can follow complicated and previously unknown pathways to reach the upper atmosphere
31 where they can be detected on the ground. This study shows a new and unusual effect where
32 some EMIC wave energy is reflected and diverted towards the equator, where it meets its
33 opposite-hemisphere counterpart, interferes with it and sets up a resonance. This resonance
34 then creates a new signal peak in the upper atmosphere at lower latitudes, far away from the
35 location of the initial source. This presents a new and hitherto unseen pathway for wave energy
36 to travel from their generation region in near-Earth space down to the ionosphere.

37 Understanding such pathways is very important for correctly diagnosing the location of these
38 wave populations in space, and assessing their role in causing reductions in the levels of space
39 radiation.

40 **Index Terms**

41 2487 Wave propagation, 2494 Instruments and techniques, 2736 Magnetosphere/ionosphere
42 interactions, 2768 Plasmasphere, 2753 Numerical modeling

43 **Keywords**

44 EMIC waves, magnetosphere, ionosphere, wave reflection, Buchsbaum resonance, field-line
45 resonances

46 **1. Introduction**

47 Electromagnetic ion cyclotron (EMIC) waves are important instabilities linked with rapid
48 radiation belt dropouts (Shprits et al., 2008). Their importance in radiation belt dynamics is an
49 active area of research and debate (e.g. Millan and Thorne, 2007, Shprits et al., 2013, 2018;
50 Mann et al., 2016, 2018). It is also known that EMIC waves can be spatially and temporally
51 localised (Usanova et al., 2010, Blum et al., 2016, 2017; Hendry et al., 2020; Kim et al., 2018a,
52 Kim et al., 2020) and can propagate in the Earth-ionosphere waveguide (e.g., Mann et al., 2014
53 and references therein). This presents a dilemma in how to effectively observe them.

54 Ground magnetometer stations (e.g. Mann et al., 2008) can provide continuous monitoring but
55 are fixed in position and their signatures are complicated by ionospheric ducting (e.g. Mann et
56 al., 2014, Kim et al., 2018b and references therein). Meanwhile, high-apogee spacecraft in
57 elliptical orbits, e.g. Van Allen Probes, Cluster, or MMS, provide limited temporal coverage as
58 they can rapidly cross the narrow L-shells supporting the EMIC waves (e.g. Usanova et al., 2008)
59 and only return to the same region on relatively long orbital timescales.

60 Meanwhile, polar low-Earth orbit (LEO) satellites, such as the European Space Agency (ESA)
61 Swarm (Friis-Christensen et al., 2008) mission, cross L-shells rapidly and thus offer the
62 possibility of higher temporal coverage. For example, Swarm A and C cross the same L-shell up
63 to four times in only 90 minutes. This makes LEO satellites potentially attractive platforms for
64 studying EMIC waves.

65 The pathway by which EMIC waves propagate from their source region to ground can be
66 complex, often involving polarization reversal, deflections at the Buchsbaum resonance
67 (Buchsbaum, 1960), mode conversion (e.g., Kim and Johnson, 2016), ionosphere waveguide
68 ducting, and possible reflection around equatorial plasma bubbles (Kim et al., 2018b). Inner
69 magnetosphere propagation models (e.g. Sydorenko and Rankin, 2012, 2013) may be used to
70 understand the correspondence between low-altitude and ground EMIC signatures and their
71 source locations farther out in the magnetosphere. These models need to be validated against
72 empirical measurements. Here we use a novel model for EMIC wave propagation to

73 demonstrate the importance of the Buchsbaum resonance in affecting the pathways by which
74 EMIC waves reach the ionosphere within the inner magnetosphere. Whereas Kim and Johnson
75 (2016) demonstrated how the Buchsbaum resonance can affect wave dynamics near their
76 equatorial generation region at $L \sim 7$, here we use a simulation domain which covers the entire
77 magnetosphere-ionosphere domain and reveal an unexpected new pathway by which EMIC
78 wave energy may reach the ionosphere at lower- L .

79 We combine data from Swarm A and C with results from this wave propagation model. Two
80 EMIC wave signal power peaks at LEO are identified in both hemispheres. The primary high-
81 latitude peak ($L \sim 3.3$) appears to represent EMIC wave power travelling straightforwardly down
82 the field line to the ionosphere. The secondary peak ($L \sim 1.7$) appears to have been generated
83 from the same source, travelling along a novel pathway from the magnetosphere to the
84 ionosphere which to our knowledge has not been reported previously. The model results show
85 compelling evidence for EMIC wave reflection through Buchsbaum resonance, followed by the
86 two reflected waves, one from each hemisphere, crossing at the equator and interfering to set
87 up resonant standing waves which pump energy into a field-line resonance (FLR), which is
88 observed as the secondary peak. Multi-spacecraft phase differencing reveals that the secondary
89 peak appears to feature strong shear-to-fast wave mode conversion.

90 **2. Data and Instrumentation**

91 The ESA Swarm mission (Friis-Christensen et al., 2008) was launched into a low-Earth polar $\sim 87^\circ$
92 orbit in 2013 and consists of three identical satellites. Swarm A and C form a pair travelling at
93 450 km altitude with a separation of 1.4° in latitude and a varying along-track separation that is
94 ~ 10 seconds apart at the time of the event. All spacecraft are equipped with the Vector
95 Fluxgate Magnetometers (VFM) sampling the magnetic field at 50 Hz (Olsen et al., 2013). The
96 coordinate system used here is the spacecraft coordinate system (VFM) where VFM_1 faces in
97 the direction of the spacecraft motion, VFM_3 faces radially upwards away from Earth, and
98 VFM_2 faces azimuthally and completes the triad. The Langmuir Probes provide plasma density
99 estimates at 16 Hz (Knudsen et al., 2017).

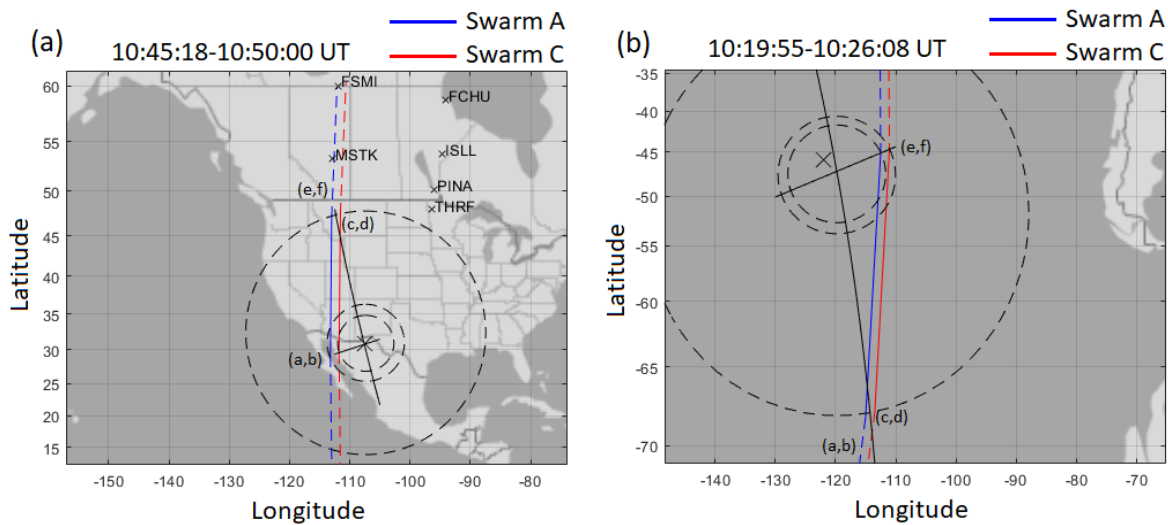
100 The Van Allen Probes pair were launched in 2012 into near-equatorial elliptical orbits with an
101 apogee of $\sim 37,000$ km and a perigee of ~ 600 km (Kessel et al., 2012). The magnetic field
102 instrument has a sampling rate of 64 samples/sec and forms part of the Electric and Magnetic
103 Field Instrument Suite (EMFISIS) (Kletzing et al., 2013).

104 The Canadian Array for Real-time InvestigationS of Magnetic Activity (CARISMA) ground-based
105 magnetometer network (Mann et al., 2008) consists of an array of induction coil
106 magnetometers (ICM) and fluxgate magnetometers (FGM), measuring magnetic field
107 perturbations on the ground across western Canada and the northern United States. The ICMs
108 and FGMs sample at 100 Hz and 8 Hz respectively.

109 **3. Results**

110 **3.1 Event Observations**

111 Swarm A/C traversed an area of intense EMIC wave activity on 17th September 2015, 10-11 UT.
 112 The pair flew northwards on the nightside through a conjugate region of EMIC wave activity
 113 spanning the southern and northern sub-auroral regions. EMIC waves (~1.5 Hz) were detected
 114 simultaneously on several CARISMA groundstations and on Swarm A/C. On Swarm, the waves
 115 were detected in both the quasi-azimuthal B_VFM_2 and |B| components. Phase differencing
 116 (Balikhin et al., 1997, Pakhotin et al., 2013) was used to estimate the source region of the
 117 compressional disturbance assuming the source location does not change on the timescale
 118 needed to traverse the area of interest, and assuming that the propagation speed of the
 119 compressional component away from the source in the duct is locally homogeneous. Figure 1
 120 displays the results of the analysis for both hemispheres. The intersection of the two black solid
 121 lines in Figure 1 (a), tracing the vectors of maximum and zero phase difference in the
 122 compressional magnetic field, allows the triangulation of the signal source, marked with a black
 123 cross. Dashed black lines denote the hypothetical isolines of compressional wave power
 124 spreading isotropically from the source. The same analysis has been applied to the southern
 125 hemisphere (Figure 1 (b)). The intersection in that hemisphere is close to the theoretical
 126 magnetic conjugate point, calculated using the IRBEM library, which is also marked as a black
 127 cross. Additional analysis assessing the impacts of potential latitudinally non-uniform
 128 propagation speeds is presented in Supplementary Material Figure S1, based on Swarm
 129 densities inferred from the Swarm Langmuir probe. However, the resulting difference in the
 130 inferred source L-shell is small.



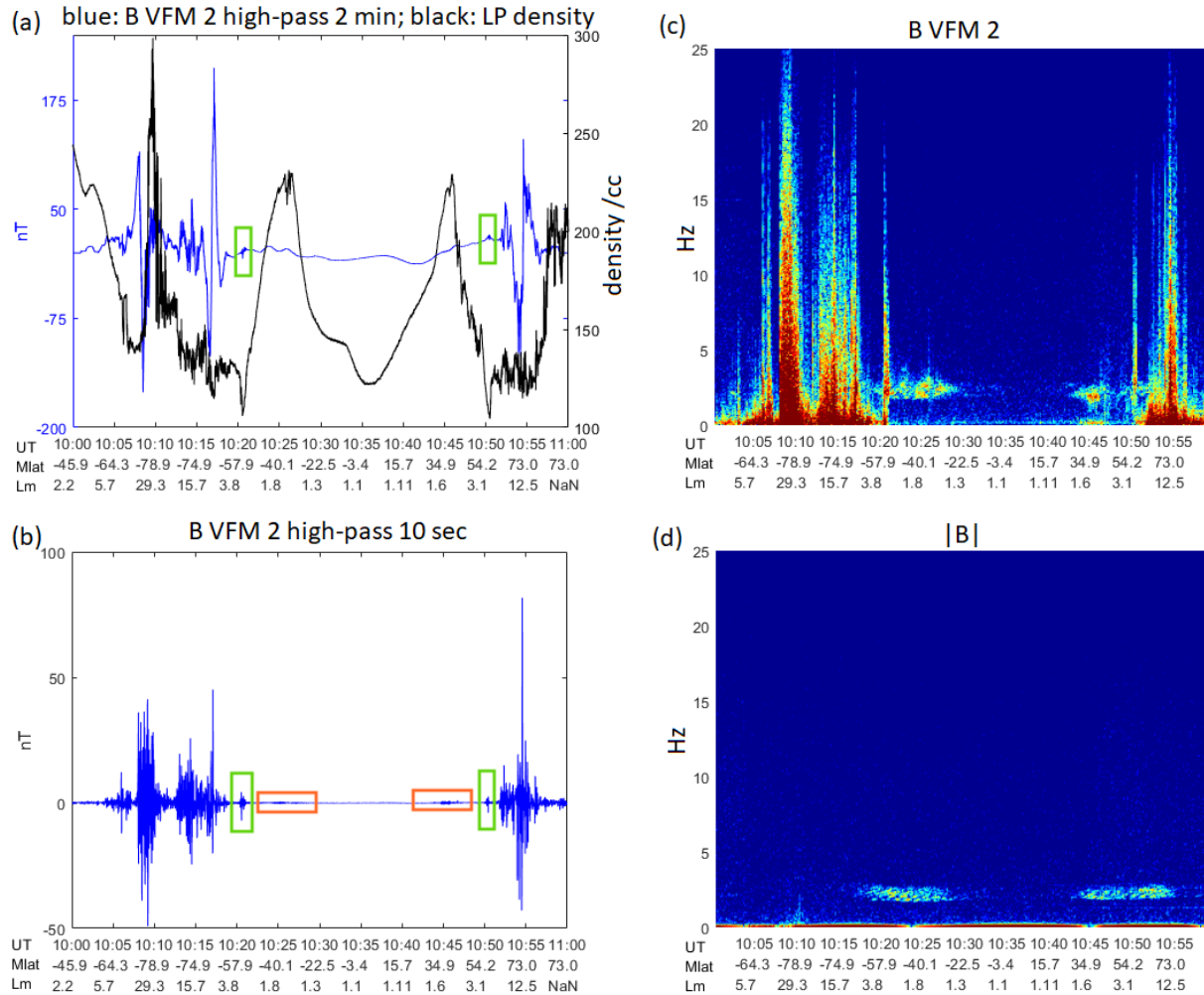
131
 132 *Figure 1: Northern (a) and southern (b) hemisphere tracks for Swarm A (SwA; blue), and Swarm*
 133 *C (SwC; red). Black solid lines denote straight lines drawn between SwA and SwC inter-*
 134 *spacecraft separation vectors at the times of maximum and zero phase differences. The*
 135 *intersection of these lines gives the approximate compressional source location. The blue and*
 136 *red traces are solid while Swarm A and C traversed the area between these zero-phase and*
 137 *max-phase locations, and dashed otherwise. Black dashed circles represent wavefronts assumed*

138 *to be spreading out omni-directionally from the source. Smaller black crosses denote CARISMA*
139 *groundstations. Large black crosses denote intersection points of the phase lines (a) and its*
140 *magnetically conjugate location (b). In the left panel, the small letter pairs (a,b), (c,d) and (e,f)*
141 *refer to the corresponding-letter panels in the waveforms shown in Figure 3 for the northern*
142 *hemisphere; in right panel the same letter pairs refer to the panels in Supplementary Figure S3*
143 *for the south.*

144 In both hemispheres, the compressional wave power appears to originate from $L \sim 1.7$. In
145 general, EMIC waves are not expected to be observed equatorially at such low L-shells (Saikin et
146 al., 2015). Van Allen Probe B (VAP-B) passed close to Swarm A/C in the equatorial plane around
147 1021 UT and neither Swarm A/C nor VAP-B observed any equatorial EMIC wave activity at 1.5
148 Hz (see Supplementary Figure S2). VAP-B, which moves in the azimuthal direction due to its
149 near-equatorial orbit, also did not see wave activity before or afterwards, despite being at
150 higher L-shells. This suggests that the event was azimuthally localized.

151 In Figure 2 (a), high-pass filtered B_VFM_2 data shows large-scale auroral-zone FACs between
152 ~ 1009 - 1018 UT in the south and ~ 1050 - 1056 UT in the north. The magnetic perturbations
153 related to EMIC waves are highlighted with green boxes, shown in more detail in Figure 2 (b)
154 where the magnetic field data has been processed with a 10s-window high-pass filter to bring
155 out the Pc1 band signal. Assuming that the plasmasphere ends where relatively large FACs
156 begin (e.g. Heilig and Lühr, 2018), the plasmopause location for both hemispheres would be
157 around $L \sim 4.7$ - 4.8 . Similarly, estimations obtained from the VAP-B EMFISIS instrument (Kletzing
158 et al., 2013), utilizing the upper hybrid frequency and density, would place the plasmopause at L
159 ~ 5 - 5.2 . These considerations would then place the Pc1 signal maxima inside the plasmasphere
160 at $L \sim 3.3$ in both hemispheres. This agrees with prior studies (e.g. Kim et al., 2018a) which show
161 EMIC waves on Swarm to be a sub-auroral phenomenon.

162 Figure 2 (c) and (d) show the transverse (B_VFM_2) and compressional ($|B|$) components of the
163 magnetic field in the frequency domain. The ~ 1.5 Hz waves are clearly seen in both
164 components, strongly suggesting in-situ mode conversion from the shear Alfvén to the
165 compressional mode. Interestingly, while the maximum wave power in the shear Alfvén mode
166 (Figure 2 (c)) appears near the assumed source location at $L \sim 3.3$ (~ 1021 UT in the south and
167 ~ 1050 UT in the north), there is also a secondary signal extending to lower latitudes in both
168 hemispheres. The maximum of this secondary signal is around 1025 UT in the south and around
169 1045 UT in the north. The secondary signal is marked in Figure 2 (b) with orange boxes. In both
170 hemispheres, wave power drops between the primary and secondary signals. The secondary
171 signal is also pronounced in the compressional component (Figure 2 (d)). The maximum wave
172 intensities of the primary peaks, in both hemispheres, are around $L \sim 3.3$. The maximum
173 intensities of the secondary peaks are at $L \sim 1.7$ - 1.8 in both hemispheres, which agrees with the
174 earlier geometric analysis in Figure 1 placing the secondary compressional Pc1 wave power
175 source at $L \sim 1.7$.



176

177 *Figure 2: For 17 Sept 2015, 10:00:00-11:00:00 UT, (a) blue shows the time series of B_VFM_2*
 178 *after the application of a 2-minute moving average high-pass filter (in nT); black shows*
 179 *Langmuir probe density, (b) shows the B_VFM_2 signal high-pass filtered with a 10-second*
 180 *moving average. The primary signal intensity maxima are marked in (a) and (b) with green*
 181 *boxes, further the secondary intensity maxima are marked on (b) with orange boxes. (c) and (d)*
 182 *show dynamic power spectra of B_VFM_2 and the B-modulus, respectively.*

183 The phase differencing methodology in the ionosphere for the secondary peak is demonstrated
 184 in detail in Figure 3, which shows the |B| readings on the spacecraft pair for three time periods.
 185 Figure 3 (a) and (b) show the magnetic perturbations around 1045 UT, where the wavepackets
 186 arrive at Swarm C before Swarm A. During the second time period, around 1050 UT (Figure 3 (c)
 187 and (d)), the wave peaks from Swarm A and C are in phase, meaning that both observe the
 188 wave simultaneously. Finally, during the third time period, around 1052 UT, shown in Figure 3
 189 (e) and (f), the lagging Swarm A observes the wave before Swarm C, meaning that the
 190 wavefronts are now catching up with the satellite pair. Similar geometric calculations were
 191 performed for the southern hemisphere (Supplementary Figure S3). In both hemispheres, the

192 inter-spacecraft wave phase changes smoothly between the three time periods, without
193 evidence of phase wrap (Supplementary Figure S4). The magnetically conjugate emission
194 regions are to the left of Swarm A/C in the south, and to the right of Swarm A/C in the north,
195 consistent with conjugate field line tracing.

196 Meanwhile, most CARISMA ICMs observe significant wave power at ~ 1.5 Hz around the time of
197 the Swarm traversals and for several hours afterwards (see Figure S5). The wave signal-to-noise
198 ratio increases with decreasing ground station latitude, suggesting that the signal source is
199 either close to THRF (L=3.6) or southwards of it. The same wave signal is also detected on other
200 CARISMA FGM stations such as Pinawa (PINA; L=4.1) and Osakis (OSAK; L=3.2), the amplitudes
201 being consistent with the L-shell of the primary wave inferred on Swarm.

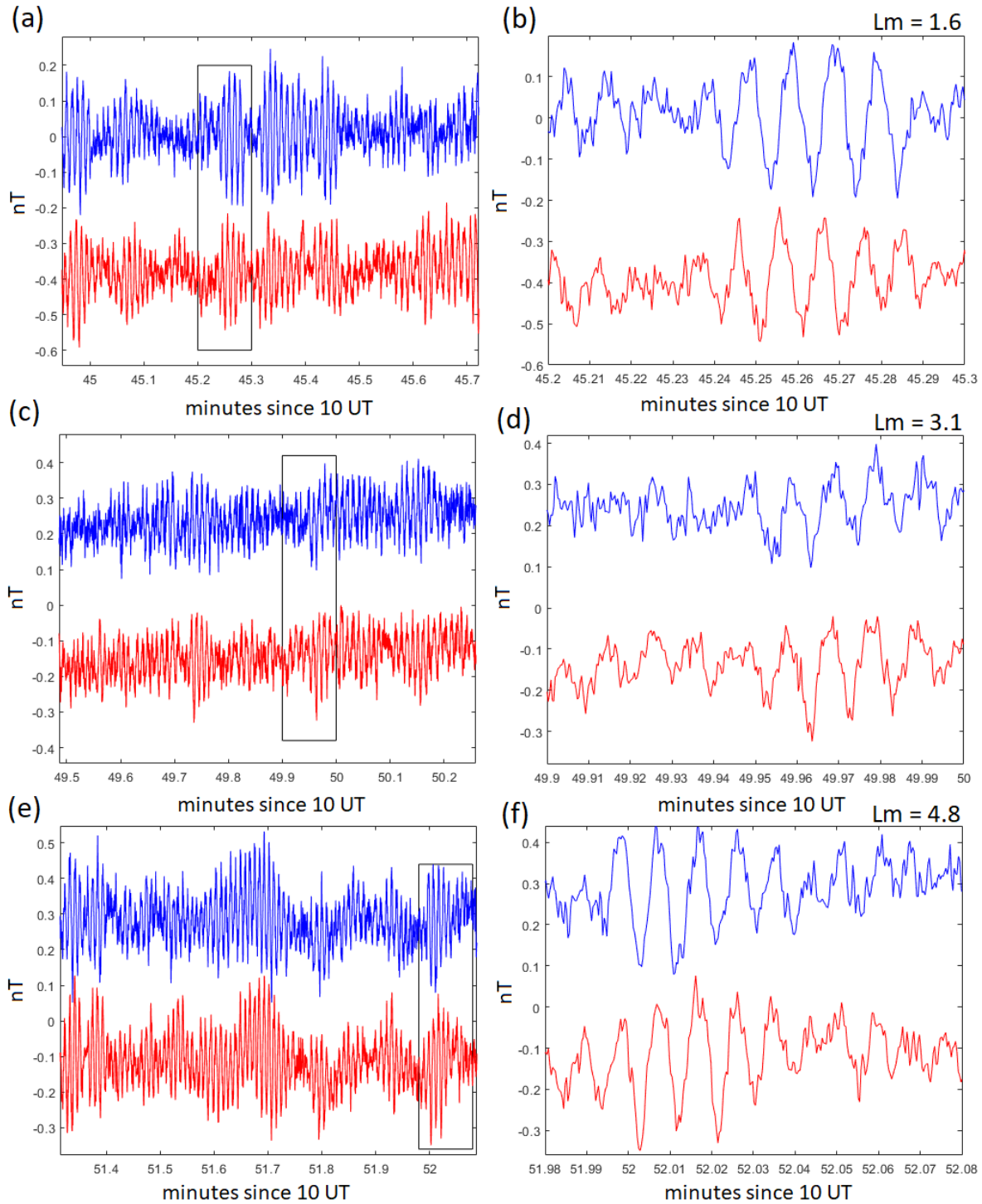
202

203

204

205

206



207

208 *Figure 3: B-field modulus readings for three time periods on Swarm A (blue) and Swarm C (red)*
 209 *as they traversed the northern hemisphere, the two time series being offset by 0.4 nT for easier*
 210 *viewing. The right column shows the areas highlighted by the black squares in the left column.*
 211 *Specifically, (a) and (b) show the period of maximum phase difference between Swarm A and C*
 212 *in the northern hemisphere, (c) and (d) show the zero-phase period, (e) and (f) show the period*
 213 *where Swarm A sees each wave front before Swarm C.*

214 **3.2 Simulation Results**

215 The event described in the present paper is simulated using a two-dimensional linear numerical
216 model of ultra-low frequency (ULF) wave propagation in atmosphere, ionosphere, and
217 magnetosphere. Equations solved by the model are presented in Supplementary Text S1.

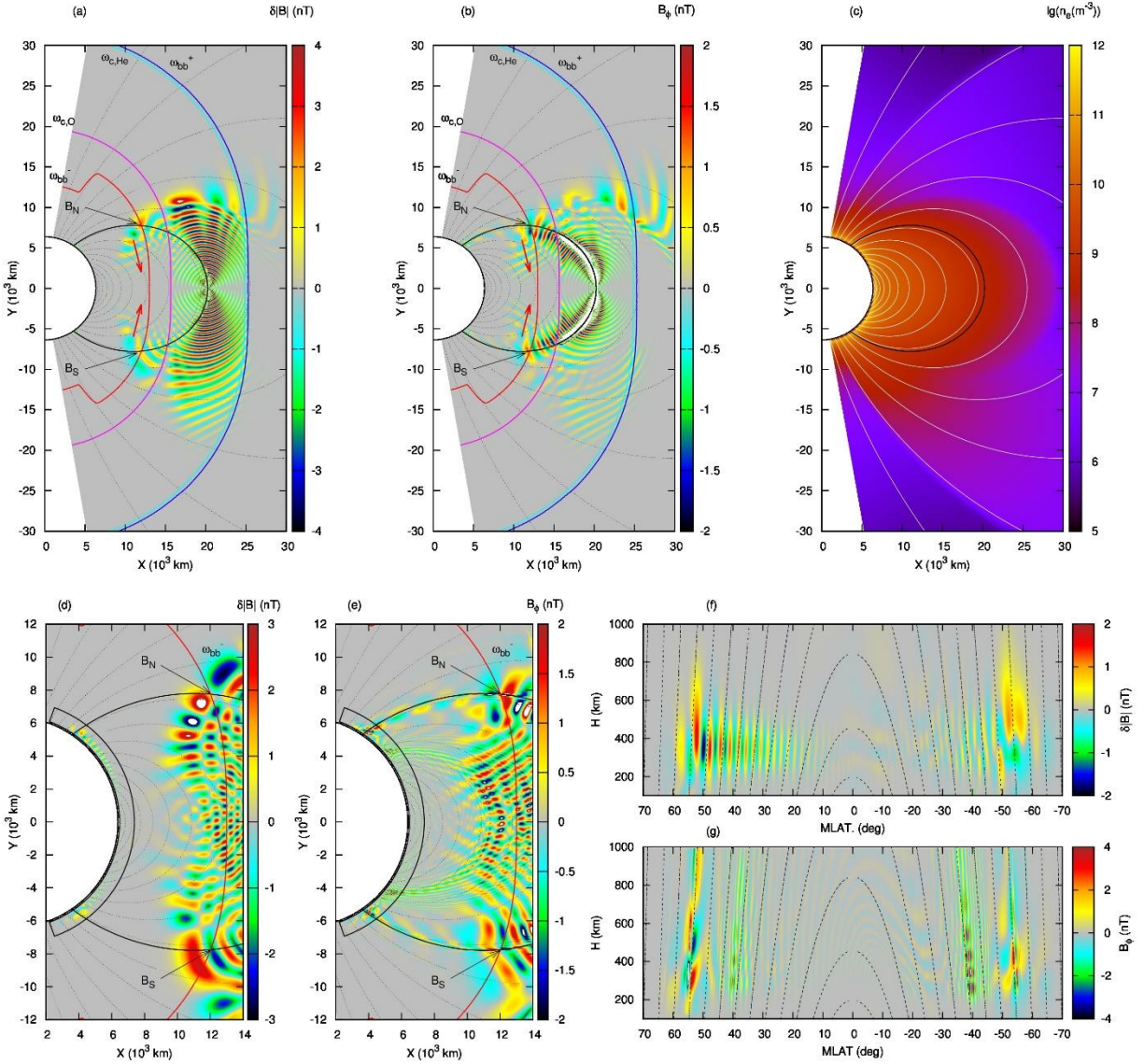
218 The simulation domain is a sector in the plane of a magnetic meridian, with the magnetic
219 latitude ranging from -80° to 80° . Spatial resolution in the radial and meridional directions is 10
220 km at the Earth surface. The inner and outer radii of the simulation domain are 6,380 km and
221 60,000 km, respectively. The ionosphere in the simulation begins at an altitude of 110 km. The
222 azimuthal wavenumber is assumed to be 40, based on the assumed azimuthal scale size of a
223 localized EMIC wave source. Parameters of ionosphere, magnetosphere, and thermosphere are
224 set using two-dimensional profiles of ion, electron, and neutral densities and temperatures
225 provided by IRI (Bilitza, 2018), GCPM (Gallagher et al, 2000), and MSIS (Hedin, 1991) for the
226 17th of September 2015, universal time 11 hours, magnetic local time 4.25 hours.

227 The wave source is an electric current loop in the meridional plane, 500 km long in the radial
228 direction and with latitudinal boundaries at $\pm 0.5^\circ$, positioned at a radius of 20,000 km in the
229 equatorial plane. The period of current oscillations in the wave source is 0.5 seconds. The
230 amplitude grows linearly for 10 seconds and then remains constant. The specific value of the
231 current amplitude in the source is of no importance since the wave model is linear. The whole
232 simulation lasts for 45 seconds. In most of the domain, the wave amplitude reaches its
233 stationary level after about 30 seconds since the beginning of the simulation.

234 Two metrics are used below to describe compressional and torsional Alfvén waves. The
235 azimuthal magnetic field perturbation, B_ϕ , which is normal to the dipole geomagnetic field and
236 therefore contributes to the variation of the magnetic field vector's direction, characterizes the
237 torsional wave. The difference between the modulus of the full magnetic field (the sum of the
238 wave perturbation \vec{B} and the geomagnetic field \vec{B}_0) and the modulus of the geomagnetic field,
239 $\delta|B| \equiv \sqrt{(\vec{B} + \vec{B}_0)^2} - B_0$, characterizes the compressional wave. Note that two movies
240 showing evolution of B_ϕ and $\delta|B|$ in space and time during the simulation are provided in
241 Supplementary Materials.

242 The spatial profile of the ion density is strongly non-uniform and includes a relatively dense
243 plasmasphere as well as a depleted plasma outside it, as shown in Figure 4(c). The wave source
244 is inside the plasmasphere. The source excites both torsional and compressional waves. The
245 torsional waves propagate along the geomagnetic field, see Figure 4(b). The compressional
246 waves propagate across the geomagnetic field, mostly towards the boundary of the
247 plasmasphere, see Figure 4(a). Compressional waves emitted by the source are ducted between
248 surfaces $\omega = \omega_{c,O}$ and $\omega = \omega_{bb}^+$, where ω is the wave frequency, $\omega_{c,O}$ is the cyclotron
249 frequency of O^+ ions, and ω_{bb}^+ is a Buchsbaum resonance frequency, see the region between
250 the magenta and the blue curves in Figure 4(a). Buchsbaum resonance frequencies ω_{bb}^\pm are

251 calculated for a 3 component plasma (H^+ , He^+ , O^+) using equation (13) of (Barbosa, 1982), the
252 plus or minus in the superscript of ω_{bb}^{\pm} corresponds to using the plus or minus in this equation,
253 respectively. Note that ω_{bb}^+ is close to the cyclotron frequency of He^+ ions $\omega_{c,He}$, compare the
254 blue and cyan curves in Figures 4(a), 4(b). In the northern hemisphere, compressional waves
255 impinging on the plasmaspheric boundary transform into waves with significant torsional
256 component propagating along the boundary on the outer side of the plasmasphere. Such a
257 process does not occur at the plasmaspheric boundary in the southern hemisphere, see Figures
258 4(a) and 4(b). The difference may be related to the magnitude of the density gradient at the
259 plasmaspheric boundary which is noticeably sharper in the northern hemisphere, as shown in
260 Figure 4(c). Waves outside the plasmasphere propagating away from the Earth are beyond the
261 scope of the present paper.



262

263 *Figure 4: Simulation results. Snapshots of the perturbation of the full magnetic field modulus (a)*
 264 *and the wave azimuthal magnetic field (b) at time $t=14.375$ sec; electron density (c);*
 265 *perturbation of the full magnetic field modulus (d,f) and the wave azimuthal magnetic field (e,g)*
 266 *at time $t=35.997$ sec. In (a,b,c,d,e), the black curve is the field line passing through the wave*
 267 *source in the equatorial plane. Gray curves in (a,b,d-g) and white curves in (c) represent dipole*
 268 *field lines crossing the Earth surface at latitudes of 80° to 10° with a 5° step. In (a,b), the*
 269 *Buchsbaum resonance surfaces $\omega = \omega_{bb}^{\pm}$ are shown by red (ω_{bb}^{-}) and blue (ω_{bb}^{+}) curves;*
 270 *surfaces $\omega = \omega_{c,O}$ and $\omega = \omega_{c,He}$ are shown by the magenta and cyan curves, respectively. In*
 271 *(d,g), red curves mark surfaces $\omega = \omega_{bb}^{-}$. In (a,b,d,e), black arrows and labels B_N and B_S mark*
 272 *locations of Buchsbaum resonances $\omega = \omega_{bb}^{-}$ on the field line of the wave source in the northern*
 273 *and southern hemispheres, respectively. In (a,b), red arrows mark equatorward propagating*
 274 *waves excited at locations $B_{N,S}$. Regions of (f,g) match the spherical slabs shown in (d,e); the*
 275 *horizontal and vertical coordinate axes in (f,g) are the latitude and altitude.*

276 Torsional waves generated by the source and propagating towards the ionosphere along the
277 geomagnetic field reach points of Buchsbaum's resonance $\omega = \omega_{bb}$ about 10.7 seconds after
278 the beginning of simulation. In Figure 4, these points are labelled B_N and B_S in the northern and
279 southern hemispheres, respectively. In the vicinity of these points, mode conversion occurs and
280 waves propagating towards the equatorial plane appear, see the regions around the red arrows
281 in Figures 4(a) and 4(b). Meanwhile, the original torsional wave continues its propagation along
282 the field line of the source (black curve in Figure 4) into the ionosphere, see Figure 4(b). After
283 about 12.2 seconds, two primary channels of wave energy entering the ionosphere form, one in
284 each hemisphere, at magnetic latitude of about 55° north and south, respectively, see Figures
285 4(b), 4(e), and 4(g).

286 Torsional waves in the primary wave channels excite compressional waves in the lower
287 ionosphere propagating equatorward inside the ionospheric waveguide, with most of the wave
288 energy confined below the altitude of about 600 km, see Figures 4(d, f). The excitation is more
289 efficient in the northern hemisphere (Figure 4 (f)), probably due to different polarization of
290 waves in the northern and southern primary channels. Meanwhile, the equatorward
291 propagating waves emitted from points of Buchsbaum resonance $B_{N,S}$ excite oscillations along
292 field lines entering the Earth surface at latitudes about 40° , see Figures 4(e) and 4(g). These
293 oscillations are standing torsional Alfvén waves, the compressional component is very weak,
294 compare figures 4(d,f) and 4(e,g). They form two secondary channels of wave energy entering
295 the ionosphere, one in each hemisphere, at time of about 20.5 seconds.

296 **4. Discussion**

297 The model results presented here demonstrate a new pathway for EMIC wave propagation
298 from a higher-L magnetosphere source to the low-L ionosphere. This pathway is generated due
299 to Buchsbaum resonance effects which reflect waves back into the lower-L magnetosphere.
300 These reflected waves interfere, creating a coherent equatorial Alfvén wave driver which
301 generates a separate peak in EMIC wave power at lower L. Whilst Kim and Johnson (2016)
302 showed how the Buchsbaum resonance can affect EMIC wave propagation at high latitudes, to
303 our knowledge our work is the first to demonstrate the importance of the Buchsbaum
304 resonance in channeling EMIC wave energy to the ionosphere.

305 Two pairs of wave channels are observed both in the model and in Swarm data – a primary at
306 $\pm 56^\circ$ magnetic latitude (MLAT) and a secondary at $\pm 38^\circ$ MLAT. Beyond 60° MLAT – the model
307 plasmaspheric boundary – the shear wave does not propagate. Swarm estimates place the
308 plasmopause $\sim 61^\circ$ MLAT. Near-equatorial wave amplitudes below 2000 km are negligible both
309 in the model and in the Swarm/VAP-B data.

310 It is not clear why, in the model, the secondary wave channels are not as efficient in
311 compressional wave excitation as the primary channels are; additional studies are needed. One
312 possible reason may be relatively large transverse and parallel wavenumbers in the secondary
313 channels, see Figure 4(g). Interestingly, it appears from multi-satellite wave vector analysis

314 (Figures 1, 3, S1, 4) that it is the secondary peak which acts as the primary wave source for
315 compressional waves. This may be due to the fact that at lower latitudes, magnetic field lines
316 are more tilted, which may increase shear-to-fast mode conversion efficiency (e.g. Sciffer et al.,
317 2004).

318 **5. Conclusions**

319 Multiple studies report on the complex relationship between space and ground Pc1 pulsations
320 (e.g. Sciffer and Waters, 2002, Lysak, 2004, Sciffer et al., 2005, Ozeke et al., 2009, Lysak et al.,
321 2013, Waters et al., 2013). The work presented here shows that the Buchsbaum resonance may
322 further complicate EMIC wave propagation in the inner magnetosphere. The model, which
323 agrees with Swarm satellite observations, clearly shows wave power from a single equatorial
324 source splitting into two intense channels due to Buchsbaum resonant reflection. The primary
325 channel travels straightforwardly down the field line, reaching the ionosphere at a similar L-
326 shell to the source region. Meanwhile, significant wave energy travels along a more complex
327 pathway: (1) Buchsbaum resonant reflection of waves towards the equator in both
328 hemispheres, (2) inter-hemispheric interference of these reflected wavefronts generating a
329 coherent driver, which (3) pumps energy into a FLR, to form a secondary field-guided channel of
330 wave energy towards the ionosphere. This secondary channel does not correspond to the L-
331 shell of wave origin, but may reach similar intensities to the primary channel.

332 This study demonstrates the importance of considering Buchsbaum resonant interactions for
333 understanding the complex dynamics of EMIC wave power transfer from an equatorial
334 generation region in the magnetosphere to the ionosphere, and which are important
335 considerations at LEO and may explain recent satellite observations of low-L EMIC waves (e.g.
336 Gamayunov et al., 2018). Given the ongoing interest in assessing the potential role of EMIC
337 waves for the loss of relativistic electrons from the radiation belts as a result of wave scattering
338 into the atmosphere (e.g., Millan and Thorne, 2007), the novel propagation pathway presented
339 here may have broader impacts for space weather as well as in general for understanding
340 instabilities in multi-ion plasmas (e.g. Stenzel et al., 2016).

341 **Data Availability Statement**

342 The ESA Swarm data can be obtained from the ESA server at swarm-diss.eo.esa.int. Van Allen
343 Probes EMFISIS data may be obtained from <https://emfisis.physics.uiowa.edu>. All equations
344 defining the model are provided in Supporting Information. The CARISMA data is available
345 online at www.carisma.ca.

346 **Acknowledgements**

347 This work was carried out under a programme of, and funded by, the European Space Agency,
348 in the frame of the ESA Living Planet Fellowship “Swarm Investigation of the Energetics of
349 Magnetosphere-Ionosphere Coupling (SIEMIC).” The view expressed in this publication can in
350 no way be taken to reflect the official opinion of the European Space Agency. The work was also

351 supported in part by the Canadian Space Agency (CSA) Class Grant “What role do Alfvén waves
352 play in energy transfer in the dynamical magnetosphere-ionosphere system?” IRM is supported
353 by a Discovery Grant from Canadian Natural Sciences and Engineering Research Council
354 (NSERC). DS is supported by the Canadian Space Agency (CSA). The ESA Swarm data can be
355 obtained from the ESA server at swarm-diss.eo.esa.int. The authors thank D.K. Milling and the
356 CARISMA team for data. CARISMA is operated by the University of Alberta, funded by the
357 Canadian Space Agency; data is available at www.carisma.ca.

358 **References**

- 359 Balikhin, M. A., deWit, T. D., Alleyne, H. S. C. K., Woolliscroft, L. J. C., Walker, S. N.,
360 Krasnosel'skikh, V., Mier-Jedrzejewicz, W. A. C., and Baumjohann, W. (1997). Experimental
361 determination of the dispersion of waves observed upstream of a quasi-perpendicular shock,
362 *Geophys. Res. Lett.*, 24, 787–790.
- 363 Barbosa, D. D. (1982), Multi-Ion Resonances in Finite Temperature Plasma, *The Astrophysical*
364 *Journal*, 254, 376-390, doi: 10.1086/159742.
- 365 Bilitza, D. (2018), IRI the International Standard for the Ionosphere, *Adv. Radio Sci.*, 16, 1-11,
366 <https://doi.org/10.5194/ars-16-1-2018>.
- 367 Blum, L. W., Agapitov, O., Bonnell, J. W., Kletzing, C., & Wygant, J. (2016). EMIC wave spatial
368 and coherence scales as determined from multipoint Van Allen Probe measurements.
369 *Geophysical Research Letters*, 43, 4799–4807. <https://doi.org/10.1002/2016GL068799>
- 370 Blum, L. W., Bonnell, J. W., Agapitov, O., Paulson, K., & Kletzing, C. (2017). EMIC wave scale size
371 in the inner magnetosphere: Observations from the dual Van Allen Probe. *Geophysical*
372 *Research Letters*, 44, 1227–1233. <https://doi.org/10.1002/2016GL072316>
- 373 Buchsbaum, S. J. (1960), Ion resonance in a multicomponent plasma, *Phys. Rev. Lett.*, 5, 495–
374 497.
- 375 Friis-Christensen, E., Lühr, H., Knudsen, D., & Haagmans, R. (2008). Swarm—An Earth
376 observation mission investigating geospace. *Advances in Space Research*, 41(1), 210–216.
377 <https://doi.org/10.1016/j.asr.2006.10.008>
- 378 Gallagher, D.L., P.D. Craven, and R.H. Comfort (2000), Global core plasma model, *J. Geophys.*
379 *Res.* 105, A8, 18 819 - 18 833, <https://doi.org/10.1029/1999JA000241>.
- 380 Gamayunov, K. V., Min, K., Saikin, A. A., & Rassoul, H. (2018). Generation of EMIC waves
381 observed by Van Allen Probes at low L shells. *Journal of Geophysical Research: Space Physics*,
382 123, 8533–8556. <https://doi.org/10.1029/2018JA025629>
- 383 Hedin, A E. (1991), Extension of the MSIS thermosphere model into the middle and lower
384 atmosphere, *J. Geophys. Res.*, 96, 1159–1172, <https://doi.org/10.1029/90JA02125>.

385 Heilig, B. and Lühr, H.: Quantifying the relationship between the plasmopause and the inner
386 boundary of small-scale field-aligned currents, as deduced from Swarm observations, *Ann.*
387 *Geophys.*, 36, 595–607, <https://doi.org/10.5194/angeo-36-595-2018>, 2018.

388 Hendry, A. T., Santolik, O., Miyoshi, Y., Matsuoka, A., Rodger, C. J., Clilverd, M. A., et al. (2020).
389 A multi-instrument approach to determining the source-region extent of EEP-driving EMIC
390 waves. *Geophysical Research Letters*, 47, 7. <https://doi.org/10.1029/2019GL086599>

391 Kessel, R. L., N. J. Fox, and M. Weiss (2012), The Radiation Belt Storm Probes (RBSP) and Space
392 Weather, *Space Sci. Rev.*, doi:10.1007/s11214-012-9953-6.

393 Kim, E.-H., and J. R. Johnson (2016), Full-wave modeling of EMIC waves near the He+
394 gyrofrequency, *Geophys. Res. Lett.*, 43, 13–21, doi:10.1002/2015GL066978.

395 Kim, H., Hwang, J., Park, J., Bortnik, J., & Lee, J. (2018a). Global characteristics of
396 electromagnetic ion cyclotron waves deduced from Swarm satellites. *Journal of Geophysical*
397 *Research: Space Physics*, 123, 1325–1336. <https://doi.org/10.1002/2017JA024888>

398 Kim, H., Hwang, J., Park, J., Miyashita, Y., Shiokawa, K., Mann, I. R., Raita, T., & Lee, J. (2018b).
399 Large-scale ducting of Pc1 pulsations observed by Swarm satellites and multiple ground
400 networks. *Geophysical Research Letters*, 45, 12,703–12,712.
401 <https://doi.org/10.1029/2018GL080693>

402 Kim, H., Shiokawa, K., Park, J., Miyoshi, Y., Hwang, J., & Kadokura, A. (2020). Modulation of Pc1
403 wave ducting by equatorial plasma bubble. *Geophysical Research Letters*, 47, e2020GL088054.
404 <https://doi.org/10.1029/2020GL088054>

405 Kletzing, C. A., et al. (2013), The Electric and Magnetic Field Instrument Suite and Integrated
406 Science (EMFISIS) on RBSP, *Space Sci. Rev.*, doi:10.1007/s11214-013-9993-6.

407 Knudsen, D. J., Burchill, J. K., Buchert, S. C., Eriksson, A. I., Gill, R., Wahlund, J.-E.,...Moffat, B.
408 (2017). Thermal ion imagers and Langmuir probes in the Swarm electric field instruments.
409 *Journal of Geophysical Research: Space Physics*, 122, 2655–2673.
410 <https://doi.org/10.1002/2016JA022571>

411 Lysak, R. L. (2004), Magnetosphere-ionosphere coupling by Alfvén waves at midlatitudes, *J.*
412 *Geophys. Res.*, 109, A07201, doi:10.1029/2004JA010454.

413 Lysak, R. L., C. L. Waters, and M. D. Sciffer (2013), Modeling of the ionospheric Alfvén resonator
414 in dipolar geometry, *J. Geophys. Res. Space Physics*, 118, 1514–1528, doi:10.1002/jgra.50090.

415 Mann, I. R., et al. (2008), The upgraded CARISMA magnetometer array in the THEMIS era, *Space*
416 *Sci. Rev.*, 141, 413–451.

417 Mann, I. R., M. E. Usanova, K. Murphy, M. T. Robertson, D. K. Milling, A. Kale, C. Kletzing, J.
418 Wygant, S. Thaller, and T. Raita (2014), Spatial localization and ducting of EMIC waves: Van

419 Allen Probes and ground-based observations, *Geophys. Res. Lett.*, 41, 785–792,
420 doi:10.1002/2013GL058581.

421 Mann, I. R., Ozeke, L. G., Murphy, K. R., Claudepierre, S. G., Turner, D. L., Baker, D. N., et al.
422 (2016). Explaining the dynamics of the ultra-relativistic third Van Allen radiation belt. *Nature*
423 *Physics*, 12(10), 978–983. <https://doi.org/10.1038/nphys3799>

424 Mann, I., Ozeke, L., Morley, S. et al. Reply to 'The dynamics of Van Allen belts revisited'. *Nat.*
425 *Phys.* 14, 103–104 (2018). <https://doi.org/10.1038/nphys4351>

426 Millan, R. M. and Thorne, R. M. (2007). Review of radiation belt relativistic electron losses. . *J.*
427 *Atmos. Sol.-Terr. Phys.* 69(3), 362–377, doi: 10.1016/j.jastp.2006.06.019

428 Olsen N, Friis-Christensen E, Floberghagen R, Alken P, Beggan CD, Chulliat A, Doornbos E, da
429 Encarnac JT, Hamilton B, Hulot G, van den IJssel J, Kuvshinov A, Lesur V, Luehr H, Macmillan S,
430 Maus S, Noja M, Olsen PEH, Park J, Plank G, Puethe C, Rauberg J, Ritter P, Rother M, Sabaka TJ,
431 Schachtschneider R, Sirol O, Stolle C, Thebault E, Thomson AWP, Toefner-Clausen L, Velimsky J,
432 Vigneron P, Visser PN (2013). The Swarm Satellite Constellation Application and Research
433 Facility (SCARF) and Swarm Data Products. *Earth Planets Space* 65. 1189–1200

434 Ozeke, L. G., I. R. Mann, and I. J. Rae (2009), Mapping guided Alfvén wave magnetic field
435 amplitudes observed on the ground to equatorial electric field amplitudes in space, *J. Geophys.*
436 *Res.*, 114, A01214, doi:10.1029/2008JA013041.

437 Pakhotin, I. P., Walker, S. N., Shprits, Y. Y., and Balikhin, M. A.: Dispersion relation of
438 electromagnetic ion cyclotron waves using Cluster observations, *Ann. Geophys.*, 31, 1437–1446,
439 <https://doi.org/10.5194/angeo-31-1437-2013>, 2013.

440 Saikin, A. A., J.-C. Zhang, R. C. Allen, C. W. Smith, L. M. Kistler, H. E. Spence, R. B. Torbert, C. A.
441 Kletzing, and V. K. Jordanova (2015), The occurrence and wave properties of H⁺, He⁺, and O⁺-
442 band EMIC waves observed by the Van Allen Probes, *J. Geophys. Res. Space Physics*, 120, 7477–
443 7492, doi:10.1002/2015JA021358.

444 Sciffer, M. D., and C. L. Waters, Propagation of ULF waves through the ionosphere: Analytic
445 solutions for oblique magnetic fields (2002), *J. Geophys. Res.*, 107(A10), 1297,
446 doi:10.1029/2001JA000184.

447 M. D. Sciffer, C. L. Waters, F. W. Menk. Propagation of ULF waves through the ionosphere:
448 Inductive effect for oblique magnetic fields. *Annales Geophysicae*, European Geosciences
449 Union, 2004, 22 (4), pp.1155-1169. hal-00317294

450 Sciffer, M. D., Waters, C. L., and Menk, F. W.: A numerical model to investigate the polarisation
451 azimuth of ULF waves through an ionosphere with oblique magnetic fields, *Ann. Geophys.*, 23,
452 3457–3471, <https://doi.org/10.5194/angeo-23-3457-2005>, 2005.

453 Shprits, Y. Y., Subbotin, D. A., Meredith, N. P., and Elkington, S. R. (2008). Review of modeling of
454 losses and sources of relativistic electrons in the outer radiation belt II: Local acceleration and
455 loss, *J. Atmos. Solar-Terr. Phys.*, 70, 1694–1713, doi:10.1016/j.jastp.2008.06.014.

456 Shprits, Y. Y., et al. (2013), Unusual stable trapping of the ultrarelativistic electrons in the Van
457 Allen radiation belts, *Nature Phys.*, doi:10.1038/nphys2760.

458 Shprits, Y., Horne, R., Kellerman, A. et al. The dynamics of Van Allen belts revisited. *Nat. Phys.*
459 14, 102–103 (2018). <https://doi.org/10.1038/nphys4350>

460 R. L. Stenzel (2016) Whistler waves with angular momentum in space and laboratory plasmas
461 and their counterparts in free space, *Advances in Physics: X*, 1:4, 687-710, DOI:
462 10.1080/23746149.2016.1240017

463 Sydorenko, D., and R. Rankin (2012), Simulation of ionospheric disturbances created by Alfvén
464 waves, *J. Geophys. Res.*, 117, A09229, doi:10.1029/2012JA017693.

465 Sydorenko, D., and R. Rankin (2013), Simulation of O⁺ upflows created by electron precipitation
466 and Alfvén waves in the ionosphere, *J. Geophys. Res. Space Physics*, 118, 5562–5578,
467 doi:10.1002/jgra.50531.

468 Usanova, M. E., Mann, I. R., Rae, I. J., Kale, Z. C., Angelopoulos, V., Bonnell, J. W., et al. (2008).
469 Multipoint observations of magnetospheric compression-related EMIC Pc1 waves by THEMIS
470 and CARISMA. *Geophysical Research Letters*, 35, L17S25.
471 <https://doi.org/10.1029/2008GL034458>

472 Usanova, M. E., et al. (2010), Conjugate ground and multisatellite observations of compression-
473 related EMIC Pc1 waves and associated proton precipitation, *J. Geophys. Res.*, 115, A07208,
474 doi:10.1029/2009JA014935.

475 Waters, C. L., Lysak, R. L., & Sciffer, M. D. (2013). On the coupling of fast and shear Alfvén wave
476 modes by the ionospheric hall conductance. *Earth, Planets and Space*, 65(5), 385-396.
477 <https://doi.org/10.5047/eps.2012.08.002>